

**Hybrid multilayer thin film supercapacitor of graphene nanosheets with polyaniline: importance of establishing intimate electronic contact through nanoscale blending†**

Taemin Lee, Taeyeong Yun, Byeongho Park, Bhawana Sharma, Hyun-Kon Song and Byeong-Su Kim\*

Received 16th May 2012, Accepted 17th August 2012

DOI: 10.1039/c2jm33111j

A hybrid electrode consisting of an electric double-layer capacitor of graphene nanosheets and a pseudocapacitor of the conducting polymer polyaniline exhibits a synergistic effect with excellent electrochemical performance for flexible thin film supercapacitors. This hybrid supercapacitor is constructed by a nanoscale blending method of layer-by-layer (LbL) assembly based on the electrostatic interactions between positively charged polyaniline (PANi) and negatively charged graphene oxide (GO) nanosheets. The hybrid electrode provides not only improved electronic conductivity through the intimate contact with the graphene nanosheet, but also enhanced chemical stability during the charge–discharge process. We also investigated the dependence of the electrochemical performance on the various parameters of LbL assembly such as the number of bilayers and the post-thermal and chemical treatments that could affect the degree of reduction of GO and PANi. We found that after thermal treatment, the LbL-assembled thin film of PANi with GO nanosheets exhibited an excellent gravimetric capacitance of  $375.2 \text{ F g}^{-1}$  at a discharge current density of  $0.5 \text{ A g}^{-1}$  that outperformed many other hybrid supercapacitors reported to date. The hybrid supercapacitor maintained its capacity up to 90.7% over 500 cycles at a high current density of  $3.0 \text{ A g}^{-1}$ . This study opens up the possibility for the production of diverse graphene-based hybrid nanocomposites that are promising for future flexible supercapacitors.

**Introduction**

With the growing demand for portable devices and electric vehicles, electrochemical capacitors, also known as supercapacitors, are garnering considerable attention as attractive electrochemical energy storage and conversion devices due to their complementary performance with respect to secondary batteries and fuel cells. A number of distinctive features such as high power density, fast charge–discharge capability, long cycle life, wide thermal operating range, and low maintenance cost clearly give supercapacitors high potential as energy storage devices.<sup>1–7</sup>

Among many promising materials used for supercapacitors, carbon-based materials have been widely employed as electrode materials due to their excellent electrical conductivity and high surface areas. In particular, graphene, a two-dimensional monolayer of an  $\text{sp}^2$ -carbon network, has recently emerged as a

new class of electrode material owing to its unique electrical, mechanical, and chemical properties, as well as its high specific surface area.<sup>8–13</sup>

Despite these favorable features, the use of graphene and related carbon materials in supercapacitors is still limited due to their low capacitance (typically in the range of  $10\text{--}10^2 \text{ F g}^{-1}$ ) and unsatisfactory performance to meet the high-power performance requirements. In order to overcome these limitations, there have been reports of preparing hybrid electrodes by combining graphene with other nanomaterials such as metal oxides and conducting polymers, thus providing the advantages of each component.<sup>14–19</sup>

Polyaniline (PANi) has been considered a promising material for energy storage and conversion with its excellent pseudocapacitive behavior, exhibiting a fast, reversible faradic reaction on the electrode surface, together with its high conductivity and ease of synthesis.<sup>20</sup> With these potential benefits, much promising research has been reported to date on combining graphene nanosheets with electrochemically active PANi, including simple solution mixing,<sup>21,22</sup> *in situ* polymerization,<sup>23–26</sup> and electropolymerization.<sup>27–29</sup> Although these recent progresses present facile routes for the fabrication of hybrid electrode films of graphene, many of the resulting hybrid films suffer from a lack of precise control over the film architecture and properties, leading

Interdisciplinary School of Green Energy and KIER-UNIST Advanced Center for Energy, Ulsan National Institute of Science and Technology (UNIST), Ulsan 689-798, Korea. E-mail: bskim19@unist.ac.kr; Tel: +82-52-217-2923

† Electronic supplementary information (ESI) available: Additional characterization data of UV/vis, XPS, and electrochemical measurements. See DOI: 10.1039/c2jm33111j

to a loss of the active surface area of the graphene sheets and intimate electrochemical interfaces necessary for maximum energy storage. Therefore, it continues to be a challenging endeavor to realize the nanoscale uniform blend of the hybrid structure of graphene nanosheets with other nanomaterials in a well-defined composition and structure.

As an alternative, one simple and versatile method for assembling a hybrid graphene structure is using layer-by-layer (LbL) assembly, which can create highly tunable, conformal thin films and functional surfaces with nanometer-scale control over the film composition and structure.<sup>30–35</sup> LbL assembly can also allow the incorporation of diverse nanostructures, including carbon nanotubes, nanoparticles, polymers, and biomolecules on virtually any surface, each with a distinct structure and composition, simply from the choice of materials and by controlling the sequence of layering.<sup>36–38</sup> The integration of graphenes into multilayer thin films has been demonstrated with LbL techniques, but the application for supercapacitors is still limited.<sup>39–43</sup>

Herein, we present the development of hybrid supercapacitors with tailored compositions and architectures that combine the concept of an electric double-layer capacitor of graphene materials and a pseudocapacitor. More specifically, by taking advantage of LbL assembly, we constructed a hybrid supercapacitor consisting of a graphene oxide (GO) nanosheet and a conducting polymer PANi based on electrostatic interactions (Scheme 1).

Because LbL-assembled PANi with graphene nanosheets has not yet been fully explored, here we carefully investigated the dependence of the electrochemical performance of hybrid thin films on the various parameters of LbL assembly, such as the number of bilayers and the post-thermal and chemical treatments that could affect the degree of reduction in GO and PANi. We also demonstrated the redox state of PANi, because it is closely related to the stability and performance of the hybrid electrode.

We found that the integration of PANi into the graphene nanosheets not only provided improved electronic conductivity and flexibility, but it also afforded a significant increase in capacitance while retaining the necessary cycle life due to the presence of graphene nanosheets. For example, the hybrid thin film supercapacitor of PANi with graphene nanosheets prepared in this study exhibits an excellent gravimetric capacitance of 375.2 F g<sup>-1</sup> at a current density of 0.5 A g<sup>-1</sup> that outperformed

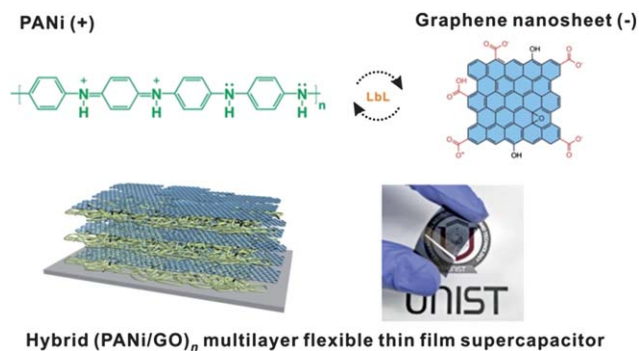
many other hybrid supercapacitors reported to date. The hybrid film also maintained up to 90.7% of its capacity over 500 cycles at a high current density of 3.0 A g<sup>-1</sup>.

## Results and discussion

To introduce the graphene nanosheet into an LbL system based on electrostatic interactions, a GO suspension was prepared from a commercial graphite powder according to the modified Hummers method.<sup>44–46</sup> Following sonication for exfoliation of the graphite oxide, the chemical functional groups introduced on the surface of the graphene sheet, such as carboxylic acids, render the prepared GO negatively charged over a wide span of pH conditions. Separately, a positively charged stable PANi suspension was prepared by dissolving an emeraldine base form of PANi ( $M_w$  20 000) in dimethylacetamide (DMAC) with subsequent dilution with pH-adjusted water (DMAC : H<sub>2</sub>O = 1 : 9 v/v) based on the literature protocol.<sup>47</sup> It should be noted that the pH window for the PANi is limited to 2.5–3.0, whereas that of GO is wide in the range of 1–12 in order for each suspension to remain stable during the assembly.

With these two stable suspensions, we fabricated the hybrid thin films by alternately dip-coating on ITO-coated glass or PET substrates or silicon wafers to afford the multilayer in the architecture of (PANi/GO)<sub>*n*</sub> (*n* = number of bilayers, typically 2–10, hereafter PG<sub>*n*</sub>) (Fig. 1). Finally, the hybrid multilayers were subjected to a further thermal reduction process under vacuum and a chemical hydrazine reduction to afford multilayers of enhanced mechanical stability and electrical conductivity following well-documented protocols.<sup>48–52</sup>

The successful growth of PG<sub>*n*</sub> multilayers was monitored from a gradual increase of the UV/vis absorbance spectra with the characteristic absorbance of each component (Fig. 1a). In addition to the absorption at 220 nm due to GO, there are two absorption bands at 319 and 458 nm originating from PANi. The peak at 319 nm can be attributed to the  $\pi$ - $\pi^*$  transition of benzenoid rings and the broad band at 458 nm is due to the polaron transition, which is a typical characteristic of the conducting emeraldine state of PANi.<sup>53,54</sup> Consistent with the UV/vis absorption spectra, the ellipsometry thickness measurements show that the thickness of the PG<sub>*n*</sub> multilayers is linearly proportional to the number of bilayers, demonstrating the uniform and well-controlled assembly of the PG<sub>*n*</sub> thin films with nanoscale precision (Fig. 1b). From the linear fitting of the



**Scheme 1** Schematic representation of layer-by-layer (LbL) assembled multilayer thin film of PANi with graphene oxide nanosheets with a photograph of the film assembled on a flexible PET substrate.

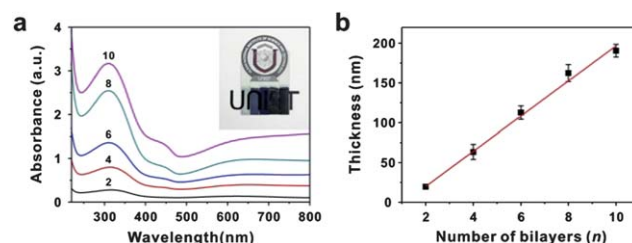


**Fig. 1** (a) UV/vis spectra and (b) ellipsometry thickness of as-assembled (PANi/GO)<sub>*n*</sub> multilayer films as a function of the number of bilayers. The number on each graph represents the number of bilayer (*n*). Inset in (a) is the image of the corresponding samples from 2- to 10-bilayer. Thickness is the average value of five independent measurements.

curves, an average bilayer thickness of *ca.* 19 nm was calculated, which is far beyond the thickness of a single layer GO nanosheet (*ca.* 0.7 nm), suggesting a non-typical superlinear growth of the multilayer films due to the interdiffusion of partially charged PANi within the multilayer films.<sup>55–59</sup> Although it is not common in the traditional LbL films of pure electrolytes, this type of superlinear growth behavior was similarly observed in the recent report by the Hammond group in which PANi nanofibers were assembled with multiwalled carbon nanotubes.<sup>52</sup>

We have further observed the tunable growth of PG<sub>n</sub> multilayers with respect to the changes in the pH of the GO suspension at a fixed pH of PANi (pH 2.5). For instance, upon increasing the pH of the GO suspensions from 3.5 to 6.5, we found that the growth of the PG<sub>n</sub> multilayer film decreased, as monitored by the UV/vis spectra (Fig. S1 in ESI†). This is due to the surface charge increase of carboxylic acid groups in the GO suspension, leading to less adsorption on the pre-adsorbed positively charged PANi layer to balance the surface charges. This type of pH-tailorable behavior of LbL thin films was similarly observed with weak polyelectrolytes, as well as with other nanomaterials, where pH can alter the degree of ionization and eventually lead to differences in the film thickness and morphology of the resulting LbL films.<sup>41,60</sup>

In order to enhance the mechanical integrity of the multilayer films to the substrate and to improve the electrical properties of the graphene nanosheets, the as-assembled hybrid multilayers of PG<sub>n</sub> were subjected to thermal reduction at 150 °C for 12 h under vacuum to yield heat-treated PG<sub>n</sub> samples (hereafter PG<sub>n</sub>-H). Additional chemical reduction of the PG<sub>n</sub>-H films *via* gaseous hydrazine monohydrate at 70 °C for 24 h afforded samples of both heat- and chemical-treated PG<sub>n</sub> (hereafter PG<sub>n</sub>-HC) with considerably enhanced electrical conductivity of the graphene nanosheets. After thermal reduction, the PG<sub>n</sub>-H films appeared dark blue, resulting from partial restoration of the conjugated aromatic structure within the graphitic structure, whereas the color of the PG<sub>n</sub>-HC films changed to dark green, reflecting the changes in the electronic state of PANi that may occur during the chemical reduction process (Fig. S2 in ESI†). The UV/vis spectra of GO in the as-assembled PG<sub>n</sub> film was also red-shifted to 275 and 268 nm after thermal and chemical reduction, respectively, which demonstrates the successful restoration of electronic conjugation within the graphene sheets.<sup>45</sup>

The side-on scanning electron microscopy (SEM) image shows the surface is covered with a uniform film of PG<sub>n</sub> multilayers (Fig. 2a and Fig. S3 in ESI†). The surface morphology of the as-assembled film exhibits characteristic wrinkled graphene sheets that are distributed over the entire film surface. The internal microstructure was investigated with transmission electron microscopy (TEM), which revealed the stacked multilayered structure of the graphene nanosheets (Fig. 2b). The elemental mapping image further supported the uniform distribution of carbon, oxygen, and nitrogen over the entire multilayer films, confirming the presence of both PANi (a source of carbon and nitrogen) and GO (a source of carbon and oxygen) within the multilayer films (Fig. 2c). The atomic force microscopy (AFM) image of the as-assembled PG<sub>n</sub> film displays a similar microstructure of the graphene sheets covered with a polymeric PANi structure without significant phase separation. Moreover, the surface morphology of the as-assembled PG<sub>10</sub> film was further

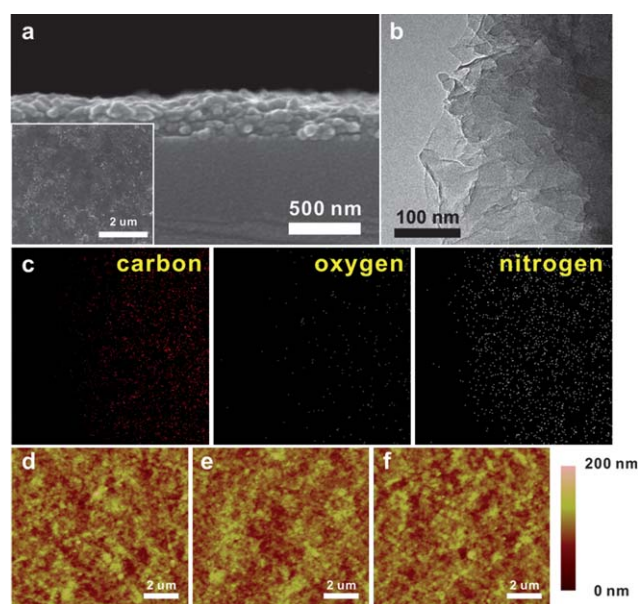


**Fig. 2** Representative images of as-assembled PG<sub>10</sub> multilayer films. (a) SEM and (b and c) TEM with a corresponding elemental mapping. Inset in (a) shows the surface morphology. (d–f) Height-mode AFM images of (d) as-assembled PG<sub>10</sub>, (e) heat treated PG<sub>10</sub>-H, and (f) both heat- and chemical-treated PG<sub>10</sub>-HC.

compared with those of PG<sub>10</sub>-H and PG<sub>10</sub>-HC (Fig. 2d–f). Although we could not determine distinctive differences in the surface morphology relating to the post-treatments, we found that the film thickness diminished significantly from  $192 \pm 3.2$  nm (PG<sub>10</sub>) to  $135 \pm 0.82$  nm (PG<sub>10</sub>-H) and  $132 \pm 0.65$  nm (PG<sub>10</sub>-HC) from ellipsometry. Similarly, the root-mean-squared surface roughness ( $R_{\text{rms}}$ ) decreased slightly from 16.7 nm (PG<sub>10</sub>) to 15.6 nm (PG<sub>10</sub>-H) and 15.7 nm (PG<sub>10</sub>-HC) after respective post-treatment processes. Taken together, the post-thermal and chemical treatments induced close packing between the PANi and GO layers *via* evaporation of intercalated water and removal of the oxygen-containing functional groups in the as-assembled PG<sub>10</sub> films.

X-ray photoelectron spectroscopy (XPS) studies were employed to monitor the progress of the characteristic binding energy of the C1s and N1s peaks corresponding to each functional group present on the graphene nanosheets and PANi (Fig. 3 and Table S1 in ESI†). On the basis of the XPS data, the atomic composition of the surface of the films was determined to be 72.93% carbon, 21.18% oxygen, and 5.89% nitrogen in the as-assembled PG<sub>10</sub> film. This survey scan allows the calculation of the relative fraction of PANi which is approximately 41.2% within the multilayer PG<sub>10</sub> film.

Deconvolution of the high-resolution spectra of C1s further affords six distinct components corresponding to the graphitic carbon framework for  $sp^2$  (C=C) (284.4 eV) and  $sp^3$  (C–C) (285.1 eV), C–N in the backbone of PANi (285.8 eV), C–O in epoxy and hydroxyl (286.6 eV), carbonyls (288.0 eV), and carboxylic acids (289.9 eV), which can be attributed to GO, as reported previously (Fig. 3a).<sup>28,61</sup> After thermal and chemical reduction treatments, the fraction of  $sp^2$ -carbon increased from 48.3 to 57.4 and 59.8%, respectively, supporting the effective recovery of the graphitic structures, as observed also in the UV/vis spectra. Moreover, it is interesting to note that the

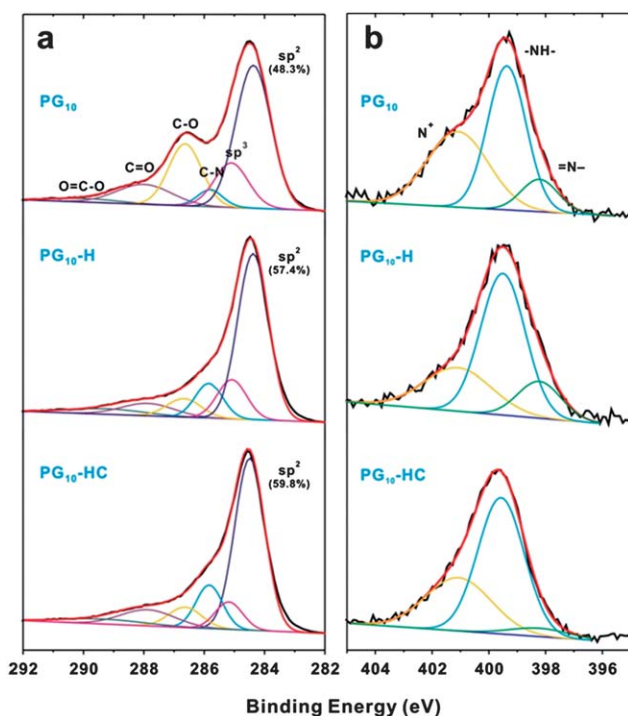


**Fig. 3** High-resolution (a) C1s and (b) N1s XPS spectra of all (PANI/GO)<sub>10</sub> multilayer films with and without post-treatments. The percentage under the sp<sup>2</sup> label in (a) represents the fraction of sp<sup>2</sup>-carbon.

composition of the C–N peak increased sharply upon chemical reduction, which is partly due to the substitution of nitrogen from the hydrazine monohydrate on the edge plane of the graphene sheets.<sup>62</sup>

In agreement with the above results, high-resolution N1s spectra further yielded detailed structural information of PANi within the multilayer. For example, Fig. 3b shows that most of the nitrogen atoms in PANi are in the form of benzenoid amine (–NH–) centered at 399.37 eV with additional small peaks, including those of quinoid imine (=N–) (398.21 eV), and positively charged nitrogen atoms (N<sup>+</sup>) (401.09 eV).<sup>63–65</sup> Although we could not observe new peaks arising after the thermal and chemical treatments, the fraction of the quinoid imine to the benzenoid amine peak (=N–/–NH–) increased modestly from 0.22 (PG<sub>10</sub>) to 0.25 (PG<sub>10</sub>-H) upon thermal treatment. On the contrary, this ratio drops drastically to 0.08 after further chemical reduction in PG<sub>10</sub>-HC, suggesting a lower overall doping level of the PANi chain in the PG<sub>10</sub>-HC film compared to that in the PG<sub>10</sub> and PG<sub>10</sub>-H films, albeit the GO is reduced accordingly. In conjunction with this observation, Maser *et al.* recently reported that the simultaneous reduction of a GO and PANi composite by hydrazine produced a solid-state charge-transfer complex possessing a lower number of quinoid groups compared to benzenoid groups.<sup>65</sup> Additionally, the relative fraction of radical cationic nitrogen at 401.09 eV decreased from 40.62 (PG<sub>10</sub>) to 27.11 (PG<sub>10</sub>-H) and 33.93% (PG<sub>10</sub>-HC), reflecting the influence of the post-thermal and chemical treatment on the doping level of the PANi structure.

To evaluate the electrochemical properties and quantify the specific capacitance of the various samples prepared in this study, we performed cyclic voltammetry (CV) measurements in 1.0 M

H<sub>2</sub>SO<sub>4</sub> electrolyte using a three-electrode configuration with platinum wire and Ag/AgCl as a counter and a reference electrode, respectively. In order to exclude the contribution of pseudocapacitive PANi within the hybrid electrode, we also assembled a (GO/GO)<sub>10</sub> multilayer electrode as a control which was composed exclusively of graphene nanosheets according to the method described in our previous reports.<sup>42,43,66,67</sup> This all-graphene multilayer of the (GO/GO)<sub>10</sub> sample was heat-treated at 150 °C for 12 h to enhance adhesion of the film to the substrate during the electrochemical cycles and to increase the conductivity of the multilayer films.

As shown in Fig. 4, all samples of the (PANI/GO)<sub>10</sub> hybrid films assembled on ITO-coated glass substrates exhibited broad redox peaks in the potential range of –0.2 to 0.8 V investigated. In particular, all hybrid electrodes displayed the typical pseudocapacitive behavior of PANi with two characteristic sets of redox peaks (C<sub>1</sub>/A<sub>1</sub> and C<sub>2</sub>/A<sub>2</sub>) related to the redox transition of PANi incorporated within the hybrid electrodes. Peaks for C<sub>1</sub>/A<sub>1</sub> are attributed to the redox transition of PANi between a semiconductive state (leucoemeraldine) and a conducting state (polaronic emeraldine), and the additional redox peaks for C<sub>2</sub>/A<sub>2</sub> are associated with the faradaic transformation of emeraldine to pernigraniline.<sup>25,27,68</sup> It is also observed that there is a positive shift of the cathodic peaks (C<sub>1</sub>/C<sub>2</sub>) and a negative shift of the anodic peaks (A<sub>1</sub>/A<sub>2</sub>) with increasing potential scan rate (Fig. S4 in ESI†). The specific capacitance (C<sub>sp</sub>) of the electrode can be calculated according to the following eqn (1):

$$C_{\text{SP}} = \frac{1}{mv(V_f - V_i)} \int_{V_i}^{V_f} I(V) dV \quad (1)$$

where *I* is the response current (A), *V<sub>f</sub>* and *V<sub>i</sub>* are the integration potential limits (V) of the voltammetric curve, *v* is the potential scan rate (V s<sup>–1</sup>), and *m* is the mass of the active electrode material measured by a quartz crystal microbalance (QCM) (g). Based on the above equation, we found a C<sub>sp</sub> of

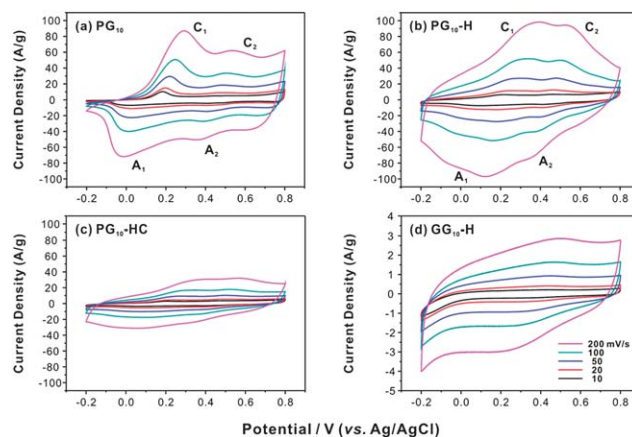


**Fig. 4** Cyclic voltammogram (CV) curves of all (PANI/GO)<sub>n</sub> hybrid electrode films with various scan rates from 10 to 200 mV s<sup>–1</sup>. (a) As-prepared PG<sub>10</sub>, (b) heat-treated PG<sub>10</sub>-H, (c) heat- and chemically-treated PG<sub>10</sub>-HC, and (d) heat-treated (GO/GO)<sub>10</sub>. All electrochemical properties were collected in a three-electrode system with a Ag/AgCl reference in 1.0 M H<sub>2</sub>SO<sub>4</sub> electrolyte at identical scan rates presented in (d). Note that the y-scale in (d) is significantly smaller than the others.

402.5–219.4 F g<sup>-1</sup> (PG<sub>10</sub>), 489.0–304.8 F g<sup>-1</sup> (PG<sub>10</sub>-H), 240.1–103.5 F g<sup>-1</sup> (PG<sub>10</sub>-HC), and 24.6–10.9 F g<sup>-1</sup> (GG<sub>10</sub>-H), respectively, at scan rates in the range of 10 to 200 mV s<sup>-1</sup> (Table S2 in ESI†). We also observed that the intermediate capacitive behavior of PG<sub>10</sub> increased upon thermal treatments to PG<sub>10</sub>-H owing to the recovery of the electrical conductivity of the graphene nanosheets, which affected the electrochemical properties of the supercapacitors. On the other hand, further chemical treatment did not improve its electrochemical performance, although the chemical reduction can effectively recover the electrical properties of the graphene nanosheets. We postulate that the chemical treatment with hydrazine can also influence the conducting level of PANi, as monitored from the relatively low ratio of quinoid imine to benzenoid amine from the XPS spectra in Fig. 3, which diminishes the electrochemical performance of the hybrid electrode. In addition, it is hard to exclude the possibility of structural degradation of PANi during the chemical reduction process.

We have also assembled different numbers of bilayers of hybrid (PANi/GO)<sub>*n*</sub> multilayers up to 40 bilayers. As expected, the overall capacitance increases with the number of bilayers; however, the specific capacitance per bilayer, as well as the cycle stability, gradually decreases beyond 10 bilayers. This suggests that a fine balance between the electron transfer from the electrode and the ionic transport from the electrolyte is important to achieve high capacitive behaviour (Fig. S5 and Table S3 in ESI†).

In clear contrast to the hybrid electrode, the assembled all-GO electrode without PANi exhibited a nearly ideal rectangular shape without any obvious redox peaks, which corresponds to a characteristic electric double-layer capacitive (EDLC) behavior with a specific capacitance of 10.9 F g<sup>-1</sup> at a scan rate of 200 mV s<sup>-1</sup>. According to the report of Hammond and Shao-Horn, multilayer thin films of all multiwalled carbon nanotubes (MWNTs) exhibit a similar rectangular capacitive behavior with a small portion of pseudocapacitive redox peaks associated with the surface functional groups attached to the surface of MWNTs such as carboxylic acid groups.<sup>69</sup>

Taken together, our hybrid system of PANi with graphene nanosheets contributed to the significant enhancement of the electrochemical performance through a synergistic effect, in which the high specific surface area and electrical conductivity of the graphene nanosheets that are coupled with the redox transition from PANi for decreased diffusion length and fast electron transfer at the interface between the electrodes and the electrolyte ions.

Fig. 5 shows the galvanostatic charge–discharge curves and specific capacitance with cyclic stability of the PG<sub>10</sub> and PG<sub>10</sub>-H hybrid electrodes as a function of discharge current density from 0.5 to 3.0 A g<sup>-1</sup>. The specific capacitance based on the galvanostat is calculated by the following eqn (2):

$$C_{\text{SP}} (\text{F g}^{-1}) = (i \times \Delta t) / \Delta E \times m \quad (2)$$

where *i* is the discharge current (A),  $\Delta t$  is discharge time (s),  $\Delta E$  is the voltage difference (V), and *m* is the active mass of electrode. According to eqn (2), we found that the thermally annealed PG<sub>10</sub>-H electrode has a much higher capacity of 116.5–375.2 F g<sup>-1</sup> than does the as-assembled PG<sub>10</sub> electrode of 94.2–162.9 F g<sup>-1</sup> over the entire range of discharge current density (0.5–3.0

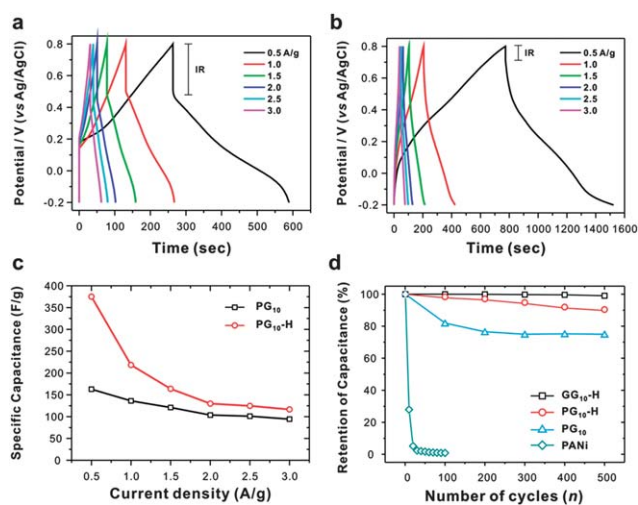


**Fig. 5** Galvanostatic charge–discharge curves of the assembled hybrid (PANi/GO)<sub>10</sub> electrodes. (a) PG<sub>10</sub>, (b) PG<sub>10</sub>-H, and (c) specific capacitance values as a function of discharge current density from 0.5 to 3 A g<sup>-1</sup>. (d) Comparison of cycling stability of all samples at a high discharge current density of 3 A g<sup>-1</sup>. Electropolymerized pure PANi film was used for comparison.

A g<sup>-1</sup>) in accord with the *C*<sub>sp</sub> measured from the CV (Table S2 in ESI†). This value is superior to several recent studies of hybrid GO and PANi structures, such as the Cheng group's freestanding paper from a reduced GO–PANi composite prepared by the electropolymerization method (233 F g<sup>-1</sup> at 20 mV s<sup>-1</sup> by CV vs 400.1 F g<sup>-1</sup> from our study),<sup>27</sup> the Shi group's composite film of rGO and PANi nanofibers by vacuum filtration (210 F g<sup>-1</sup> at 0.3 A g<sup>-1</sup>),<sup>22</sup> and the Baek group's PANi-grafted reduced GO (250 F g<sup>-1</sup> at 100 mV s<sup>-1</sup> by CV vs 323.8 F g<sup>-1</sup> from our study) (Table S4 in ESI†).<sup>70</sup> Moreover, based on the above values, we calculated that the energy density of each PG<sub>10</sub> and PG<sub>10</sub>-H electrodes reach 18.92 and 30.34 Wh kg<sup>-1</sup>, respectively, at a power density of 1.0 kW kg<sup>-1</sup> (see Ragone plot in Fig. S6 in ESI†).

It is of note that the thermally annealed PG<sub>10</sub>-H electrode showed a lower IR drop during the discharge compared to that of the PG<sub>10</sub> electrode, clearly indicating the close packed structure and improved electrical conductivity of the active materials *via* thermal reduction effectively decreased the internal resistance in the assembled hybrid electrode. It has also been suggested that a well-ordered nanostructure can reduce the ionic diffusion path, facilitate ionic motion to the inside of the film, and improve the utilization of the electrode materials.<sup>71,72</sup> Due to the instability and lack of adhesion to the substrate of PG<sub>10</sub>-HC during repeated charge–discharge cycles, we could not obtain reproducible data for PG<sub>10</sub>-HC, unfortunately.

Furthermore, we examined the cycling stability of the prepared hybrid electrodes using a galvanostatic charge–discharge test. Interestingly, the PG<sub>10</sub>-H electrode demonstrates a considerably better cycling stability up to 500 cycles with 90.7% retention of the initial capacitance compared to that of the as-assembled PG<sub>10</sub> electrode (78.4% retention) at a discharge current density of 3 A g<sup>-1</sup>. It should be noted that although the capacitance retention of the pure GO multilayer film is still better after 500 cycles (99.8%), the preservation of the capacitive behavior of the hybrid electrode is radically improved when compared with that

of pure electropolymerized PANi (only 28.3% after mere 10 cycles) (Fig. 5d and Fig. S7 in ESI†). These results suggest that the presence of a partially reduced graphene nanosheet within the hybrid electrode not only improved the electrical conductivity, but also served as a functional dopant to PANi with an enhanced chemical stability during the charge–discharge process, thereby contributing to the excellent electrochemical performance for supercapacitors.

## Conclusions

In conclusion, we have developed a simple method of fabricating hybrid thin film supercapacitors of polyaniline (PANi) and graphene oxide (GO) nanosheets by nanoscale blending layer-by-layer (LbL) assembly based on electrostatic interactions. The hybrid electrode prepared by the LbL method not only offers precise control over the thickness, internal structure and flexibility, but also enhanced chemical stability and electronic conductivity during the charge–discharge process, benefiting from each component synergistically. We found that the LbL-assembled PANi with GO nanosheets thin film after thermal treatment could exhibit an excellent gravimetric capacitance of  $375.2 \text{ F g}^{-1}$  at a  $0.5 \text{ A g}^{-1}$  discharge current density that outperformed many other hybrid supercapacitors reported to date and maintained its capacity up to 90.7% over 500 cycles at a high current density of  $3.0 \text{ A g}^{-1}$ . The current work highlights how LbL assembly can be applied to produce nanoscale intimate interfaces at the electroactive blends of graphene nanosheets with polymeric materials. We anticipate that this platform technique will offer the potential to address critical questions on the fundamental relationship between structure and energy storage properties, as well as bridging the performance gap that currently exists between batteries and capacitors for the future.

## Experimental section

### Preparation of polyaniline (PANi) suspension

The polyaniline suspension was prepared by the method reported previously.<sup>47</sup> The emeraldine base form of polyaniline ( $M_w$  20 000, Aldrich) was dissolved in dimethylacetamide (DMAc) at a concentration of  $20 \text{ mg mL}^{-1}$  by stirring the solution overnight and then bath sonicating for 10 h. The fine particulates were removed by filtering the solution through plain filter paper. The polyaniline dipping solution was prepared by slowly adding one part (by volume) of the filtered polyaniline solution to nine parts of pH-adjusted water (pH 3.0). The pH was then quickly lowered to 2.5 by adding a few drops of 1.0 M HCl solution. The solution was filtered through a  $0.45 \text{ }\mu\text{m}$  filter again prior to use. The polyaniline dipping solutions were typically used within 2 days of preparation, as they otherwise form irreversible aggregates.

### Preparation of graphene oxide (GO) suspension

Graphite oxide was synthesized from graphite powder (Aldrich,  $<20 \text{ }\mu\text{m}$ ) by the modified Hummers method and exfoliated to give a brown dispersion of graphene oxide (GO) under ultrasonication. The GO powder dissolved in a known volume of water is subjected to ultrasonication for 40 min to give a stable suspension of GO (typically conc.  $0.50 \text{ mg mL}^{-1}$ ) and then

centrifuged at 4000 rpm for 10 min to remove any aggregates remaining in the suspension.

### Fabrication of layer-by-layer assembled (PANi/GO)<sub>n</sub> multilayer films

We prepared the two solutions of opposite charges of PANi and GO with pH 2.5 and 3.5 adjusted by 0.1 M HCl, respectively. The as-cleaned substrates were first dipped into a PANi solution for 15 min and then washed in three baths of deionized water (pH 2.5) for 1 min each, to remove residuals and weakly adsorbed PANi. Then, the substrates were dipped into a GO solution for 15 min and washed in the same way with deionized water adjusted to pH 3.5. This cycle makes one bilayer of PANi/GO film, and controls the thickness and formation by repeating the cycles from nanometer to micrometer scale. To enhance the mechanical stability and electrical conductivity of the assembled PANi/GO films, we annealed the as-prepared samples at  $150 \text{ }^\circ\text{C}$  for 12 h in a vacuum oven. To further improve the graphene properties, we conducted a vapor chemical reduction by using hydrazine monohydrate ( $\text{N}_2\text{H}_4 \cdot \text{H}_2\text{O}$ ) at  $70 \text{ }^\circ\text{C}$  for 24 h with  $\text{N}_2$  flow.

### Fabrication of electropolymerized PANi electrode

Aniline monomer was *in situ* electropolymerized on an ITO-coated glass substrate in aqueous 1.0 M  $\text{H}_2\text{SO}_4$  electrolyte containing 0.5 M aniline by a cyclic potential sweep between  $-0.6$  and  $1.4 \text{ V}$  versus a saturated calomel electrode (SCE) at a scan rate of  $100 \text{ mV s}^{-1}$ .<sup>73</sup> After electropolymerization, the PANi electrode was extensively washed with deionized water and dried. The degree of polymerization of PANi could be controlled by the number of potential sweep cycles. After 20 cycles, the electropolymerized PANi film has  $69.23 \text{ }\mu\text{g cm}^{-2}$  active mass, which was calculated with a quartz crystal microbalance. The galvanostatic charge–discharge curves were conducted in 1.0 M  $\text{H}_2\text{SO}_4$  aqueous electrolyte in the range from  $-0.2$  to  $0.8 \text{ V}$  vs an Ag/AgCl reference electrode with  $3 \text{ A g}^{-1}$  of constant discharge current density for 500 cycles.

### Preparation of electrodes and electrochemical measurements

(PANi/GO)<sub>n</sub> films were assembled on an ITO-coated glass substrate and were directly used as a working electrode in a three-electrode test cell. Platinum wire and Ag/AgCl were used as a counter and reference electrode, respectively. The characterization of the electrochemical performance for the as-prepared PG<sub>n</sub> electrode was conducted using a VMP3 electrochemical potentiostat (BioLogic Inc.). Cyclic voltammograms (CVs) and the galvanostatic charge–discharge process were measured with a potential window from  $-0.2$  to  $0.8 \text{ V}$  versus Ag/AgCl in 1.0 M  $\text{H}_2\text{SO}_4$  aqueous electrolyte with wide scan rates from 10 to  $200 \text{ mV s}^{-1}$  and a discharge current density from  $0.5$  to  $3 \text{ A g}^{-1}$ . We also conducted quartz crystal microbalance (QCM) measurements to acquire the active mass on the electrode, depending on the number of bilayers and post-treatments. The active mass can be calculated using the following Sauerbrey equation:

$$\Delta \text{mass} = \frac{-\Delta \text{freq} \times A \times \sqrt{\mu_q \times \rho_q}}{2 \times F_q^2} \quad (3)$$

$$\Delta_{\text{mass}} = -\Delta_{\text{freq}} \times 5.453 \times A \quad (4)$$

where  $\Delta_{\text{mass}}$  is the mass change (g),  $\Delta_{\text{freq}}$  is the resonant frequency change (Hz),  $\mu_{\text{q}}$  is AT-cut quartz crystal constant ( $2.947 \times 10^{11} \text{ g cm}^{-1} \text{ s}^{-2}$ ),  $\rho_{\text{q}}$  is the quartz crystal density ( $2.648 \text{ g cm}^{-3}$ ),  $F_{\text{q}}$  is the reference frequency (9.00 MHz), and  $A$  is the surface area of the electrode ( $\text{cm}^2$ ). The active mass of the electrodes of annealed (GO/GO)<sub>10</sub>, as-prepared (PANi/GO)<sub>10</sub>, and heat treated (PANi/GO)<sub>10</sub> are 1.35, 43.63, and 38.81  $\mu\text{g}$  within a specific area ( $1.4 \text{ cm}^2$ ), respectively. Consequently, the specific capacitance can be calculated by dividing the gravimetric capacitance by a specific surface area.

### Other characterization methods

The growth and structure of the (PANi/GO)<sub>n</sub> films were analyzed using UV/vis absorption spectra (Varian, Cary 5000) and X-ray photoelectron spectroscopy (XPS, Thermo Fisher, K-alpha). The thickness of the as-prepared samples on the silicon substrates was measured by ellipsometry (J. A. Woollam Co. Inc., EC-400 and M-2000V). The surface morphology of the prepared electrodes was examined using an atomic force microscope (AFM, Dimension D3100, Veeco) *via* tapping mode and the surface morphology and interior structure of the hybrid films of (PANi/GO)<sub>n</sub> were investigated using a field emission scanning electron microscope (FESEM, FEI, Nanonova 230) and a transmission electron microscope (TEM, JEOL JEM-2100, accelerating voltage of 200 kV, Gatan CCD camera).

### Acknowledgements

This research was supported by the WCU (World Class University) program through the Korea Science and Engineering Foundation funded by the Ministry of Education, Science and Technology (R31-2008-000-20012-0) and also by the National Research Foundation of Korea (NRF) grant (2010-0003219).

### Notes and references

- 1 B. E. Conway, *J. Electrochem. Soc.*, 1991, **138**, 1539–1548.
- 2 R. Kotz and M. Carlen, *Electrochim. Acta*, 2000, **45**, 2483–2498.
- 3 E. Frackowiak and F. Beguin, *Carbon*, 2001, **39**, 937–950.
- 4 A. S. Arico, P. Bruce, B. Scrosati, J. M. Tarascon and W. Van Schalkwijk, *Nat. Mater.*, 2005, **4**, 366–377.
- 5 R. F. Service, *Science*, 2006, **313**, 902.
- 6 P. Simon and Y. Gogotsi, *Nat. Mater.*, 2008, **7**, 845–854.
- 7 L. L. Zhang and X. S. Zhao, *Chem. Soc. Rev.*, 2009, **38**, 2520–2531.
- 8 K. S. Novoselov, A. K. Geim, S. V. Morozov, D. Jiang, Y. Zhang, S. V. Dubonos, I. V. Grigorieva and A. A. Firsov, *Science*, 2004, **306**, 666–669.
- 9 S. Stankovich, D. A. Dikin, G. H. B. Dommett, K. M. Kohlhaas, E. J. Zimney, E. A. Stach, R. D. Piner, S. T. Nguyen and R. S. Ruoff, *Nature*, 2006, **442**, 282–286.
- 10 A. K. Geim and K. S. Novoselov, *Nat. Mater.*, 2007, **6**, 183–191.
- 11 J. Wu, W. Pisula and K. Müllen, *Chem. Rev.*, 2007, **107**, 718–747.
- 12 C. Lee, X. Wei, J. W. Kysar and J. Hone, *Science*, 2008, **321**, 385–388.
- 13 K. S. Kim, Y. Zhao, H. Jang, S. Y. Lee, J. M. Kim, K. S. Kim, J.-H. Ahn, P. Kim, J.-Y. Choi and B. H. Hong, *Nature*, 2009, **457**, 706–710.
- 14 D. Wang, D. Choi, J. Li, Z. Yang, Z. Nie, R. Kou, D. Hu, C. Wang, L. V. Saraf, J. Zhang, I. A. Aksay and J. Liu, *ACS Nano*, 2009, **3**, 907–914.
- 15 S. Biswas and L. T. Drzal, *Chem. Mater.*, 2010, **22**, 5667–5671.
- 16 S.-S. Li, K.-H. Tu, C.-C. Lin, C.-W. Chen and M. Chhowalla, *ACS Nano*, 2010, **4**, 3169–3174.
- 17 D. H. Wang, R. Kou, D. Choi, Z. G. Yang, Z. M. Nie, J. Li, L. V. Saraf, D. H. Hu, J. G. Zhang, G. L. Graff, J. Liu, M. A. Pope and I. A. Aksay, *ACS Nano*, 2010, **4**, 1587–1595.
- 18 H. Wang, L. F. Cui, Y. Yang, H. Sanchez Casalongue, J. T. Robinson, Y. Liang, Y. Cui and H. Dai, *J. Am. Chem. Soc.*, 2010, **132**, 13978–13980.
- 19 H. Bai, C. Li and G. Shi, *Adv. Mater.*, 2011, **23**, 1089–1115.
- 20 J. Jang, *Adv. Polym. Sci.*, 2006, **199**, 189–260.
- 21 H. Bai, Y. Xu, L. Zhao, C. Li and G. Shi, *Chem. Commun.*, 2009, 1667–1669.
- 22 Q. Wu, Y. Xu, Z. Yao, A. Liu and G. Shi, *ACS Nano*, 2010, **4**, 1963–1970.
- 23 Y. Matsuo, T. Niwa and Y. Sugie, *Carbon*, 1999, **37**, 897–901.
- 24 J. Xu, K. Wang, S.-Z. Zu, B.-H. Han and Z. Wei, *ACS Nano*, 2010, **4**, 5019–5026.
- 25 K. Zhang, L. L. Zhang, X. S. Zhao and J. Wu, *Chem. Mater.*, 2010, **22**, 1392–1401.
- 26 L. Q. Xu, Y. L. Liu, K.-G. Neoh, E.-T. Kang and G. D. Fu, *Macromol. Rapid Commun.*, 2011, **32**, 684–688.
- 27 D.-W. Wang, F. Li, J. Zhao, W. Ren, Z.-G. Chen, J. Tan, Z.-S. Wu, I. Gentile, G. Q. Lu and H.-M. Cheng, *ACS Nano*, 2009, **3**, 1745–1752.
- 28 X. M. Feng, R. M. Li, Y. W. Ma, R. F. Chen, N. E. Shi, Q. L. Fan and W. Huang, *Adv. Funct. Mater.*, 2011, **21**, 2989–2996.
- 29 M. Xue, F. Li, J. Zhu, H. Song, M. Zhang and T. Cao, *Adv. Funct. Mater.*, 2012, **22**, 1284–1290.
- 30 G. Decher, *Science*, 1997, **277**, 1232–1237.
- 31 F. Caruso, R. A. Caruso and H. Möhwald, *Science*, 1998, **282**, 1111–1114.
- 32 F. Caruso, *Adv. Mater.*, 2001, **13**, 11–22.
- 33 J. W. Ostrander, A. A. Mamedov and N. A. Kotov, *J. Am. Chem. Soc.*, 2001, **123**, 1101–1110.
- 34 P. T. Hammond, *Adv. Mater.*, 2004, **16**, 1271–1293.
- 35 J. Hong, J. Y. Han, H. Yoon, P. Joo, T. Lee, E. Seo, K. Char and B.-S. Kim, *Nanoscale*, 2011, **3**, 4515–4531.
- 36 J. F. Rusling, E. G. Hvashtkovs, D. O. Hull and J. B. Schenkman, *Chem. Commun.*, 2008, 141–154.
- 37 C. Lee, I. Kim, H. Shin, S. Kim and J. Cho, *Nanotechnology*, 2010, **21**, 185704.
- 38 T. Nakashima, J. Zhu, M. Qin, S. Ho and N. A. Kotov, *Nanoscale*, 2010, **2**, 2084–2090.
- 39 N. A. Kotov, I. Dékány and J. H. Fendler, *Adv. Mater.*, 1996, **8**, 637–641.
- 40 N. I. Kovtyukhova, P. J. Ollivier, B. R. Martin, T. E. Mallouk, S. A. Chizhik, E. V. Buzaneva and A. D. Gorchinskiy, *Chem. Mater.*, 1999, **11**, 771–778.
- 41 T.-K. Hong, D. W. Lee, H. J. Choi, H. S. Shin and B.-S. Kim, *ACS Nano*, 2010, **4**, 3861–3868.
- 42 H. Hwang, P. Joo, M. S. Kang, G. Ahn, J. T. Han, B.-S. Kim and J. H. Cho, *ACS Nano*, 2012, **6**, 2432–2440.
- 43 S. H. Yang, T. Lee, E. Seo, E. H. Ko, I. S. Choi and B.-S. Kim, *Macromol. Biosci.*, 2012, **12**, 61–66.
- 44 W. S. Hummers and R. E. Offeman, *J. Am. Chem. Soc.*, 1958, **80**, 1339.
- 45 D. Li, M. B. Muller, S. Gilje, R. B. Kaner and G. G. Wallace, *Nat. Nanotechnol.*, 2008, **3**, 101–105.
- 46 J.-S. Lee, T. Lee, H.-K. Song, J. Cho and B.-S. Kim, *Energy Environ. Sci.*, 2011, **4**, 4148–4154.
- 47 J. H. Cheung, W. B. Stockton and M. F. Rubner, *Macromolecules*, 1997, **30**, 2712–2716.
- 48 S. Stankovich, D. A. Dikin, R. D. Piner, K. A. Kohlhaas, A. Kleinhammes, Y. Jia, Y. Wu, S. T. Nguyen and R. S. Ruoff, *Carbon*, 2007, **45**, 1558–1565.
- 49 S. W. Lee, B.-S. Kim, S. Chen, Y. Shao-Horn and P. T. Hammond, *J. Am. Chem. Soc.*, 2008, **131**, 671–679.
- 50 X. F. Gao, J. Jang and S. Nagase, *J. Phys. Chem. C*, 2010, **114**, 832–842.
- 51 V. C. Tung, M. J. Allen, Y. Yang and R. B. Kaner, *Nat. Nanotechnol.*, 2009, **4**, 25–29.
- 52 M. N. Hyder, S. W. Lee, F. Ç. Cebeci, D. J. Schmidt, Y. Shao-Horn and P. T. Hammond, *ACS Nano*, 2011, **5**, 8552–8561.
- 53 S.-A. Chen and G.-W. Hwang, *J. Am. Chem. Soc.*, 1995, **117**, 10055–10062.
- 54 K. Sheng, H. Bai, Y. Sun, C. Li and G. Shi, *Polymer*, 2011, **52**, 5567–5572.

- 55 P. Lavalle, V. Vivet, N. Jessel, G. Decher, J.-C. Voegel, P. J. Mesini and P. Schaaf, *Macromolecules*, 2004, **37**, 1159–1162.
- 56 J. F. Quinn, J. C. C. Yeo and F. Caruso, *Macromolecules*, 2004, **37**, 6537–6543.
- 57 P. J. Yoo, K. T. Nam, J. Qi, S.-K. Lee, J. Park, A. M. Belcher and P. T. Hammond, *Nat. Mater.*, 2006, **5**, 234–240.
- 58 C. Porcel, P. Lavalle, G. Decher, B. Senger, J. C. Voegel and P. Schaaf, *Langmuir*, 2007, **23**, 1898–1904.
- 59 N. S. Zacharia, D. M. DeLongchamp, M. Modestino and P. T. Hammond, *Macromolecules*, 2007, **40**, 1598–1603.
- 60 S. S. Shiratori and M. F. Rubner, *Macromolecules*, 2000, **33**, 4213–4219.
- 61 L. Tang, Y. Wang, Y. Li, H. Feng, J. Lu and J. Li, *Adv. Funct. Mater.*, 2009, **19**, 2782–2789.
- 62 S. Park, Y. Hu, J. O. Hwang, E.-S. Lee, L. B. Casabianca, W. Cai, J. R. Potts, H.-W. Ha, S. Chen, J. Oh, S. O. Kim, Y.-H. Kim, Y. Ishii and R. S. Ruoff, *Nat. Commun.*, 2012, **3**, 638.
- 63 F. Fusalba and D. Bélanger, *J. Phys. Chem. B*, 1999, **103**, 9044–9054.
- 64 C.-C. Hu and J.-Y. Lin, *Electrochim. Acta*, 2002, **47**, 4055–4067.
- 65 C. Vallés, P. Jiménez, E. Muñoz, A. M. Benito and W. K. Maser, *J. Phys. Chem. C*, 2011, **115**, 10468–10474.
- 66 J. Hong, K. Char and B.-S. Kim, *J. Phys. Chem. Lett.*, 2010, **1**, 3442–3445.
- 67 D. W. Lee, T.-K. Hong, D. Kang, J. Lee, M. Heo, J. Y. Kim, B.-S. Kim and H. S. Shin, *J. Mater. Chem.*, 2011, **21**, 3438–3442.
- 68 F. Montilla, M. A. Cotarelo and E. Morallon, *J. Mater. Chem.*, 2009, **19**, 305–310.
- 69 S. W. Lee, N. Yabuuchi, B. M. Gallant, S. Chen, B.-S. Kim, P. T. Hammond and Y. Shao-Horn, *Nat. Nanotechnol.*, 2010, **5**, 531–537.
- 70 N. A. Kumar, H.-J. Choi, Y. R. Shin, D. W. Chang, L. Dai and J.-B. Baek, *ACS Nano*, 2012, **6**, 1715–1723.
- 71 Y. G. Wang, H. Q. Li and Y. Y. Xia, *Adv. Mater.*, 2006, **18**, 2619–2623.
- 72 H. Zhang, G. Cao, Z. Wang, Y. Yang, Z. Shi and Z. Gu, *Electrochem. Commun.*, 2008, **10**, 1056–1059.
- 73 D. Sazou and C. Georgolios, *J. Electroanal. Chem.*, 1997, **429**, 81–93.